Hidden Lewis acidity: Studies on the medium and structure dependent fluorescence of zinc(II) complexes

Hannah Kurz,[a] Gerald Hörner,[a] Oskar Weser,[b] Giovanni Li Manni,[b] Birgit Weber*[a]

[a] H. Kurz, Dr. G. Hörner, Prof. Dr. B. Weber
Inorganic Chemistry IV
University of Bayreuth
Universitätsstraße 30, 95447 Bayreuth, Germany
E-mail: weber@uni-bayreuth.de
[b] O. Weser, Dr. G. Li Manni
Max Planck Institute for Solid State Research
Heisenbergstraße 1, 70569 Stuttgart, Germany

Supporting information for this article is given via a link at the end of the document.

Abstract: Three new zinc(II) coordination units **[Zn(1–3)]** based on planar-directing tetradentate Schiff base-like ligands **H_2(1–3)** were synthesized. Their solid-state structures were investigated by single crystal X-ray diffraction, showing the tendency to overcome the square-planar coordination sphere by axial ligation. Affinity in solution towards axial ligation has been tested by extended spectroscopic studies, both in the absorption and emission mode. The electronic spectrum of the pyridine complex **[Zn(1)(py)]** has been characterized by multiconfiguration pair-DFT to validate the results of extended TD-DFT studies. Green emission of fluorescence-silent solutions of **[Zn(1–3)]** in chloroform could be switched on in the presence of potent Lewis-bases. While interpretation in terms of an equilibrium of stacked/non-fluorescent and destacked/fluorescent species is in line with precedents from literature, the sensitivity of **[Zn(1–3)]** was greatly reduced. Results of a computation-based structure search allow to trace the hidden Lewis acidity of **[Zn(1–3)]** to a new stacking motif, resulting in a strongly enhanced stability of the dimers.

Introduction

Switchable materials are of great interest for applications as molecular sensor materials.[1] These materials need to combine a high sensitivity toward external physical or chemical stimuli with an easily detectable change of discrete properties such as photoluminescence. For this purpose, metal complexes with photoluminescent ligands are an interesting class of materials, as they can combine an easily tunable photoluminescence based on the ligand with a switching behavior based on the metal center. Various switching processes are possible that depend on the metal center and its electronic configuration. One possibility is the switching based on externally induced spin transitions. Two well-known phenomena are *spin crossover* (SCO), which is mostly investigated for $3d^6$ iron(II) complexes,[2] and *coordination induced spin state switching* (CISSS) that can be observed with $3d^8$ nickel(II) complexes.[3] In recent years, many workgroups focused on combining one of these two switching mechanisms with a photoluminescent ligand to obtain emissive sensor materials.[4] Therefore, an electronic coupling of the metal with the ligand is elementary. However, this coupling often results in non-radiative deactivation independent on the spin state due to low lying *d-d* states.[5]
Due to these drawbacks, recently much emphasis was put on metal centers with closed d^0 or d^{10} shells such as Zr(IV), Cu(I), or Zn(II). As the *d* orbitals of the metal center are not directly electronically involved in the photophysical processes, the emission is not quenched and a wide range of photoluminescent complexes has been reported.[5b,6] Especially, zinc(II) complexes are interesting for the application as molecular sensor materials, as their emission is often medium dependent. In the last decade many zinc(II) complexes have been reported that show aggregation-induced emission enhancement (AIEE).[7]
Interestingly, the opposite case – an emission quenching due to stacking – has been observed as well with zinc(II) complexes. Many studies focus on zinc(II) complexes based on a Schiff base tetradentate ligand equipped with nitrile substituents.[8] Coordination of additional ligands resulted in a strong increase of the emission intensity. Experimental and computational studies suggested that the zinc(II) complexes stack into dimers or oligomers in non-coordinating solvents.[8d,8f] The high emission intensity increase in coordinating solvents was assigned to de-stacking of the zinc(II) complexes.[8b,8d] This effect was used previously for bioimaging and biosensing in living cells.[8c,8g,9] Furthermore, derivatives of this zinc(II) complex type were investigated for their mechanochromic luminescence behavior, and as emitters for optical temperature sensing via thermally activated delayed fluorescence (TADF).[10]
Herein, we present a concerted experiment-theory approach to investigate the influence of the molecular structure on the fluorescence of zinc(II) complexes. A family of neutral complexes of Schiff base-like ligands with appended nitrile groups **[Zn(L)X]** (for the nature of **L**, see Scheme 1; **X** = H_2O, EtOH, THF, py) was synthesized. Please note that the short-cut **[Zn(1–3)]** is used whenever the nature of the axial ligand cannot be specified. In agreement with the established stacking/destacking hypothesis put forward by Di Bella and others for analogue Schiff-base derived

complexes,[8d,8f] turn-on emission behavior is observed in spectroscopic titrations with Lewis-bases, but requires much higher base loads. The seemingly weakened Lewis-base affinity of **[Zn(L)X]** was found to be due to sterically hidden Lewis-acidity based on the formation of highly stable dimers in non-coordinating solvents. Results from (time-dependent) density functional theory are benchmarked through complete active space self-consistent field methods. CASSCF, followed by the multi-configurational pair-density functional theory correction (MC-PDFT) accurately captures correlation effects for the relevant states involved in the diagnostic ILCT process.

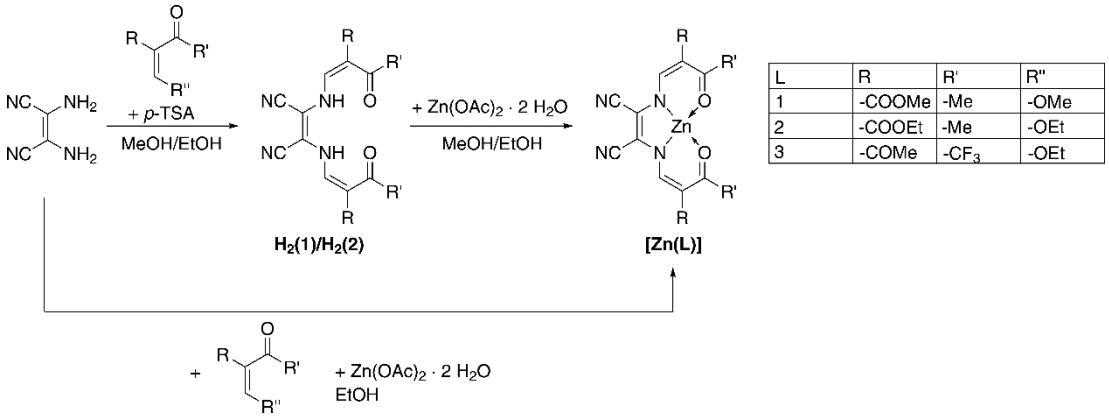

L	R	R'	R''
1	-COOMe	-Me	-OMe
2	-COOEt	-Me	-OEt
3	-COMe	-CF_3	-OEt

Scheme 1. Synthetic pathway toward the reported zinc(II) coordination units **[Zn(1–3)].**

Results and Discussion

Complex syntheses and characterization.

The zinc(II) coordination units **[Zn(1)]** and **[Zn(2)]** were synthesized in two steps as shown in Scheme 1; **[Zn(3)]** was synthesized in a one-pot reaction as the synthesis of the free ligand **H_2(3)** failed. In the case of **H_2(1)** and **H_2(2)** the free Schiff base-like ligands were obtained directly through reaction of diaminomaleonitrile with the respective keto-enol ether in the presence of *p*-toluenesulfonic acid (*p*-TSA); **H_2(2)** has been reported previously.[11] **H_2(1)** was received from MeOH as an orange solid in 44% yield. The identity and purity of the ligands was confirmed by ^{1}H NMR spectroscopy, mass spectrometry, and elemental analysis. It is noted that resonances of the NH hydrogen atom could not be observed spectroscopically, neither in IR nor ^{1}H NMR. This finding indicates fast exchange in solution and strong involvement of the NH hydrogen atoms in a hydrogen bond network in the solid.
From the ligands the respective zinc(II) complexes were obtained through turnover with stoichiometric $Zn(OAc)_2{\cdot}2\,H_2O$ in alcohol media. Thereby, acetate provides the required base equivalents. In this manner **{[Zn(1)](H_2O)(MeOH)}** and **{[Zn(2)]$_2$(H_2O)$_3$}** were obtained as a red crystalline (70 %) and an orange solid (47%), respectively. **{[Zn(3)](H_2O)(EtOH)}** was received as an orange solid (66%) in a zinc-templated three-component reaction in EtOH (diaminomaleonitrile, keto-enol ether, $Zn(OAc)_2{\cdot}2\,H_2O$; 1:2.2:1.3). Sample homogeneity and purity was established by ^{1}H NMR spectroscopy and mass spectrometry. Elemental analysis indicated the presence of stoichiometrically defined amounts of solvent molecules in the samples as indicated by the above empirical formulae. X-ray diffraction of single-crystalline samples indeed identified the complexes to be five (N_2O_3) and six-coordinate (N_2O_4) in the solid, besides additional solvent molecules in the lattice.

X-ray diffraction analysis

Molecular structures and packing pattern were addressed by single-crystal X-ray diffraction. The crystallographic data of all crystal structures are summarized in Table S1/S2 in the SI. Orange block-like crystals of **[Zn(1)(MeOH)]·MeOH** were obtained directly from the mother liquor. The material crystallises in the orthorhombic space group *Pbca*. The asymmetric unit consists of the five-coordinate zinc(II) complex and one solvent MeOH molecule as shown in Figure 1A (see Figure S1 for a fully labelled representation of the asymmetric unit). The zinc(II) centre is enclosed in a close-to-ideal tetragonal pyramidal N_2O_3 coordination sphere (S_p(SqPy) = 1.18),[12] wherein an axial methanol ligand adds to the N_2O_2 chelate cycles of the Schiff base-like ligand. Selected bond lengths are given in Table 1. The average bond lengths within the chelate cycle are 1.99 Å ($Zn1–O_{eq}$), 2.06 Å ($Zn1–N_{eq}$), and 2.01 Å ($Zn1–O_{ax}$). The *cis*-angles including the zinc(II) metal center are in the range of 97–104°, which indicates an almost ideal square-pyramidal coordination sphere.
Yellow plate-like crystals of **[Zn(1)(py)]** were obtained by adding deuterated pyridine to a solution of **{[Zn(1)](H_2O)(MeOH)}** in deuterated acetonitrile. In the triclinic space group $P\bar{1}$, the asymmetric unit consists of

one five-coordinate zinc(II) complex as shown in Figure 1B (see Figure S2 for a fully labelled representation of the asymmetric unit). The zinc(II) centre is enclosed in a N_3O_2 coordination sphere due to an axially coordinating pyridine molecule. The bond lengths (2.01 Å ($Zn1–O_{eq}$), 2.06 Å ($Zn1–N_{eq}$), 1.99 Å ($Zn1–N_{ax}$),) are very similar to the ones of **[Zn(1)(MeOH)]·MeOH**. However, the square-pyramidal coordination sphere features a slightly higher distortion with bond angles of 94–110° (S_p(SqPy) = 2.07).[12] A very similar asymmetric unit with five-coordinate zinc(II) complexes could be obtained by crystallization from wet acetonitrile. Thereby, orange rhombohedral-like crystals of **[Zn(1)(H_2O)]** were obtained that crystallize in the triclinic space group $P\bar{1}$. The asymmetric unit consists of a five-coordinate zinc(II), where one water molecule acts as the axial ligand leading to a N_2O_3 coordination sphere (see Figure 1C and Figure S3 in the SI for a fully labelled representation of the asymmetric unit). The average bond lengths are with 2.00 Å ($Zn1–O_{eq}$), 2.06 Å ($Zn1–N_{eq}$), and 2.06 Å ($Zn1–O_{ax}$) very similar to the ones of **[Zn(1)(MeOH)]·MeOH**. However, similar to **[Zn(1)(py)]**, the square-pyramidal coordination sphere shows a slightly higher degree of distortion (S_p(SqPy) = 1.97).[12]

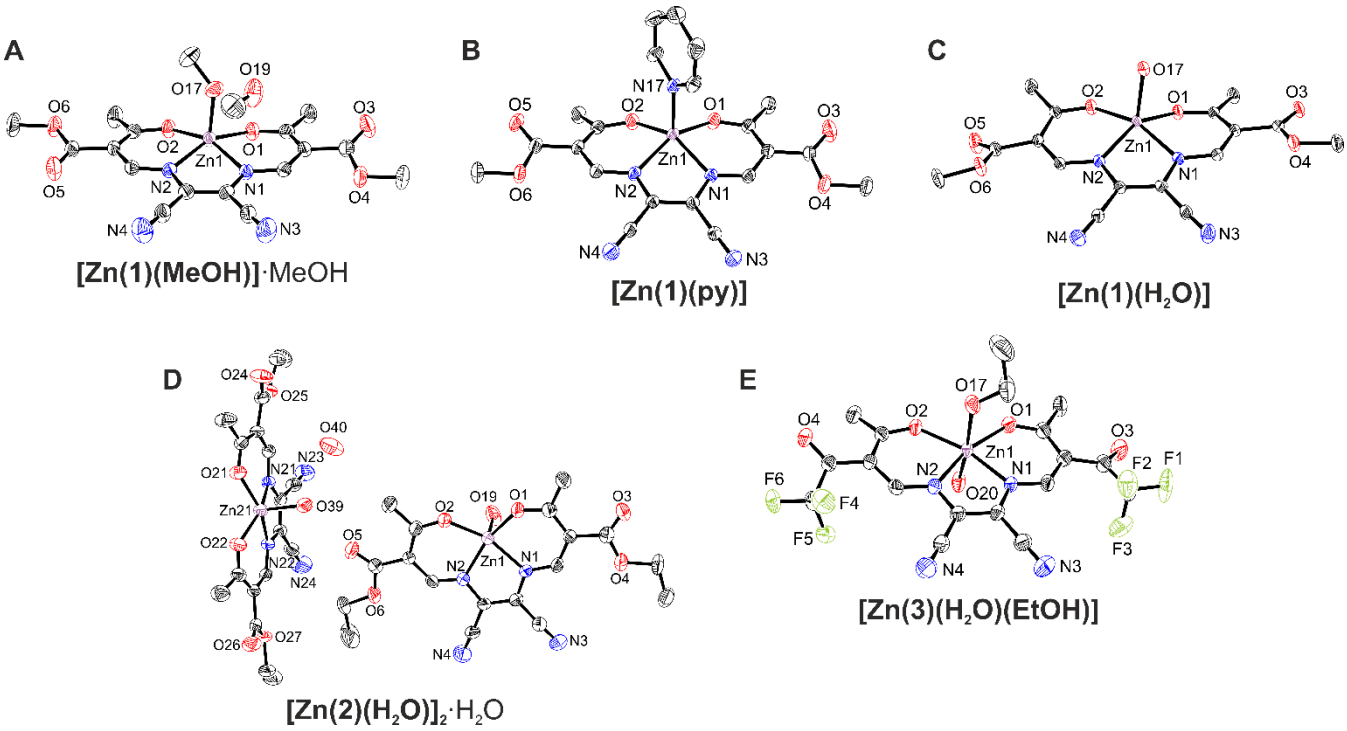

Figure 1. Structures of the asymmetric units of **[Zn(1)(MeOH)]·MeOH** (A), **[Zn(1)(py)]** (B), **[Zn(1)(H_2O)]** (C), **[Zn(2)(H_2O)]$_2$·H_2O** (D), and **[Zn(3)(H_2O)(EtOH)]** (E). Hydrogen atoms are omitted for clarity. Ellipsoids are shown at 50% probability level.

Similar to **[Zn(1)(MeOH)]·MeOH**, the zinc(II) centre in **[Zn(2)(H_2O)]$_2$·H_2O** is enclosed in a N_2O_3 coordination sphere where water ligates axially. Orange block-like single crystals of **[Zn(2)(H_2O)]$_2$·H_2O** obtained from the mother liquor were analysed in the triclinic space group $P\bar{1}$. The asymmetric unit consists of two five-coordinate zinc(II) complexes and one water solvent molecule (see Figure 1D and Figure S4 for a fully labelled representation of the asymmetric unit). The bond lengths and angles (2.00 Å ($Zn1–O_{eq}$), 2.06 Å ($Zn1–N_{eq}$), 1.99 Å ($Zn1–O_{ax}$), 99–104°) of the largely undistorted square-pyramidal coordination sphere (S_p(SqPy) = 1.28/1.36)[12] closely match the data of **[Zn(1)(MeOH)]·MeOH**. Interestingly, the metrics of all these complexes closely mimic structures which have been reported of five-coordinate zinc(II) complexes deriving from *salmant* (2,2'-[(1,2-Dicyanoethene-1,2-diyl)bis-(nitrilomethanylylidyne)]-diphenol)[13] and *salophen* (2,2'-[1,2-Phenylenebis(nitrilomethyl-idyne)]diphenol) ligands.[14]

Finally, red block-like crystals of **[Zn(3)(H_2O)(EtOH)]** were obtained from the mother liquor. Different from **[Zn(1/2)]**, fragment **[Zn(3)]** exhibits electron withdrawing CF_3 substituents. This increase in acidity of the zinc(II) metal centre is directly reflected in a coordination of two axial ligands leading to a six-coordinate zinc(II) complex. In the monoclinic space group $P2_1/c$, the asymmetric unit consists of one mononuclear six-coordinate zinc(II) complex, where the axial positions are occupied by one water and one EtOH ligand (see Figure 1E and Figure S5 in the SI for a fully labelled representation of the asymmetric unit). This coordination results in an N_2O_4 coordination sphere. The average bond lengths (2.05 Å ($Zn1–O_{eq}$), 2.09 Å ($Zn1–N_{eq}$), 2.12 Å ($Zn1–O_{ax}$)) are significantly longer than in

the five-coordinate congeners **[Zn(1)(MeOH)]** and **[Zn(2)(H_2O)]**. The O_{ax}-Zn1-O_{ax} *trans*-angle of 166.53(16) and *cis*-angles of 85–87° indicate a distorted octahedral coordination sphere ($S_p(O_h)$ = 1.83)[12].

Table 1. Selected bond lengths [Å] and bond angles [°] of **[Zn(1)(MeOH)]·MeOH**, **[Zn(1)(py)]**, **[Zn(1)(H_2O)]**, **[Zn(2)(H_2O)]$_2$·H_2O**, and **[Zn(3)(H_2O)(EtOH)]**.

Compound	Bond	Bond length	Bonds	Bond angle
[Zn(1)(MeOH)]·MeOH	Zn1-O_{eq}	1.9925(15) 1.9909(15)	O_{eq}-Zn1-O_{eq}	99.21(6)
	Zn1-N_{eq}	2.0562(18) 2.0572(18)	N_{eq}-Zn-O_{ax}	97.78(7) 103.77(7)
	Zn1-O_{ax}	2.0091(19)	O_{eq}-Zn-O_{ax}	97.15(7) 103.34(7)
[Zn(1)(py)]	Zn1-O_{eq}	2.0060(18) 2.0074(16)	O_{eq}-Zn1-O_{eq}	93.86(7)
	Zn1-N_{eq}	2.0708(18) 2.0576(19)	N_{eq}-Zn1-N_{ax}	110.08(7) 108.28(8)
	Zn1-N_{ax}	2.0480(18)	O_{eq}-Zn1-N_{ax}	99.31(7) 101.00(7)
[Zn(1)(H_2O)]	Zn1-O_{eq}	2.0117(11) 1.9866(11)	O_{eq}-Zn1-O_{eq}	98.92(4)
	Zn1-N_{eq}	2.0577(12) 2.0624(12)	N_{eq}-Zn-O_{ax}	102.68(5) 112.45(5)
	Zn1-O_{ax}	2.0555(12)	O_{eq}-Zn-O_{ax}	96.41(5) 97.30(5)
[Zn(2)(H_2O)]$_2$·H_2O	Zn1-O_{eq}	2.000(3) 2.003(3)	O_{eq}-Zn1-O_{eq}	99.36(12)
	Zn1-N_{eq}	2.062(3) 2.055(3)	N_{eq}-Zn-O_{ax}	102.30(15) 103.35(16)
	Zn1-O_{ax}	1.991(5)	O_{eq}-Zn-O_{ax}	99.19(15) 100.36(15)
[Zn(3)(H_2O)(EtOH)]	Zn1-O_{eq}	2.057(3) 2.043(3)	O_{eq}-Zn1-O_{eq} O_{ax}-Zn1-O_{ax}	111.90(12) 166.53(16)
	Zn1-N_{eq}	2.090(4) 2.098(4)	O_{eq}-Zn-$O_{ax,EtOH}$	87.12(13) 86.91(14)
	Zn1-O_{ax}	2.129(4) 2.108(4)	O_{eq}-Zn-$O_{ax,H2O}$	85.91(13) 85.02(14)

In the crystal, *π*-*π* interactions between the chelate cycles Zn1–N1–C4–C5–N2 of neighbouring complexes and towards the zinc(II) metal centre result in stacking into *dispersion dimers*, both in **[Zn(1)(MeOH)]** and **[Zn(2)(H_2O)]** (see Figure 2 and Figure S7 in the SI; Table S3 in the SI for distances and angles of the *π*-*π* and M-*π* interactions). These * dispersion dimers* interact with neighboring molecules through a hydrogen bond network, where the coordinated ROH and the lattice ROH are strongly involved (see Figure S6 in the SI; Table S4 in the SI for hydrogen bond and angles). In the case of **[Zn(2)(H_2O)]$_2$·H_2O** these stacking effects and the hydrogen bond network involving all water molecules result in a zigzag structure in the molecular packing (see Figure S8 in the SI; Table S4 in the SI for hydrogen bond and angles).

A similar molecular packing was observed for **[Zn(1)(H_2O)]**, where *π*-*π* interactions between the chelate cycle and the zinc(II) metal of neighbouring molecules results as well in *dispersion polymers* (see Figure S9 in the SI). Furthermore, a hydrogen bond chain is formed, where the hydrogens of the axial water ligand act as donor towards the carboxylic oxygen O3 and the nitrile nitrogen N4 (see Figure S10 in the SI). The supramolecular packing in **[Zn(1)py]** clearly differs from the above cases, as no dispersion dimers are observed due to the coordination of pyridine. The packing is dominated by non-classical hydrogen bonds forming columns. Two molecules are interacting through a non-classical hydrogen bond from the hydrogen H11B to the carboxylic oxygen O4. Furthermore, a second interaction of each molecule to another molecule is based on a hydrogen bond of H20

acting as donor towards the carboxylic oxygen O3. These columns are interacting with other columns through *π-π* interactions of the oxygen O3 with a pyridine ring of a molecule from another column (see Figure S11 in the SI; Table S3/4 in the SI).

In the case of **[Zn(3)(H$_2$O)(EtOH)]** the packing is likewise dominated by hydrogen bonds resulting in a 3D hydrogen bond network, with the hydrogen H20A of the axial water ligand acting as a donor towards carboxylic oxygen O4. A second hydrogen bond between these thus connected zinc(II) complexes involves the hydrogen H17 of the axial ethanol ligand acting as a donor towards the carboxylic oxygen O3. These classical hydrogen bonds lead to the formation of complex columns, which are linked together through additional hydrogen bonds involving the hydrogen H20B of the axial water ligand and the nitrile nitrogen N4 (see Figure S12 in the SI; Table S4 in the SI for hydrogen bond and angles).

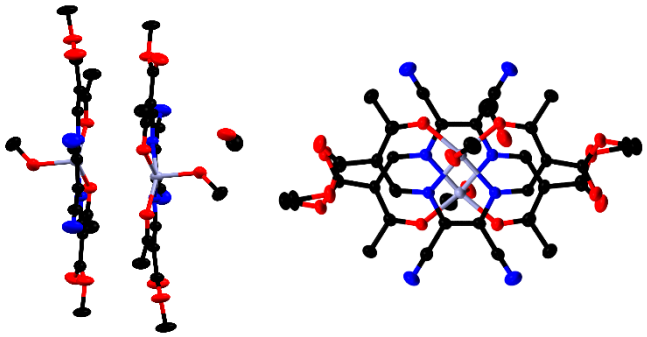

Figure 2. Representation of the stacking into *dimers* of and **[Zn(1)(MeOH)]·MeOH** from different angles. Hydrogen bonds are omitted for clarity. Ellipsoids are shown at 50% probability level.

Powder X-ray diffraction patterns of the zinc(II) complexes **[Zn(2/3)]** at RT are matched by the calculated patterns of **[Zn(2/3)]** based on the single-crystals data (Figure S13 in the SI), indicating conserved formulations of bulk and crystalline samples. In contrast, the calculated pattern of **[Zn(1)]** clearly differs from the experimental data, as could be expected from the different constitution of bulk powder and single crystal.

Optical properties of the zinc(II) complexes

Steady-state absorption and emission. Due to the closed shell character and a large net nuclear charge, zinc(II) centers of coordination compounds usually interfere with direct electronic involvement in optical processes such as absorption or emission. In particular, radiative transitions with predominating MLCT character that are the basis of the rich photophysics and photochemistry of copper(I) are prohibited in isoelectronic zinc complexes. Instead, optical excitation and relaxation are largely dominated by the ligand. Nevertheless, coordination of zinc(II) by the deprotonated ligands **(1)** and **(2)** clearly affects the optical properties in solution as they are strongly red-shifted going from a yellow to an orange solution.
Accordingly, the optical spectra are dominated by intense absorption bands centered at 413 nm (ε_M = 3.9/3.6 · 10^4 $M^{-1}cm^{-1}$) and 467 nm (ε_M = 3.6 · 10^4 $M^{-1}cm^{-1}$) for dilute solutions in chloroform (c = 7·10^{-6} M) of the ligands **H$_2$(1/2)** and the zinc complexes **[Zn(1/2)]**, respectively. The leading absorption in **[Zn(3)]** bearing CF_3 substituents is located at 451 nm (see Figure 3A and Figure S14/15 in the SI). Exemplarily, this distinct red shift upon coordination by Δv = 2800 cm^{-1} is shown for ligand **H$_2$(1)** and **[Zn(1)]** in Figure 3A; similar observations hold for **H$_2$(2)/[Zn(2)]** (Fig. S14B and S15A in the SI). The strong UV band in the ligand spectrum at 305 nm is likewise shifted to smaller energy by Δv = 2100 cm^{-1}. Spectral shifts of ligand-centered bands upon coordination are not unique. For a topologically related couple deriving from salicylic aldehyde, a coordination-dependent red shift has been recorded from 374 nm (in acetonitrile) for the ligand[15] to 560 nm for the zinc complex (in DMSO)[16]; that is, excitation energy shifts by as much as Δv = 8800 cm^{-1}.

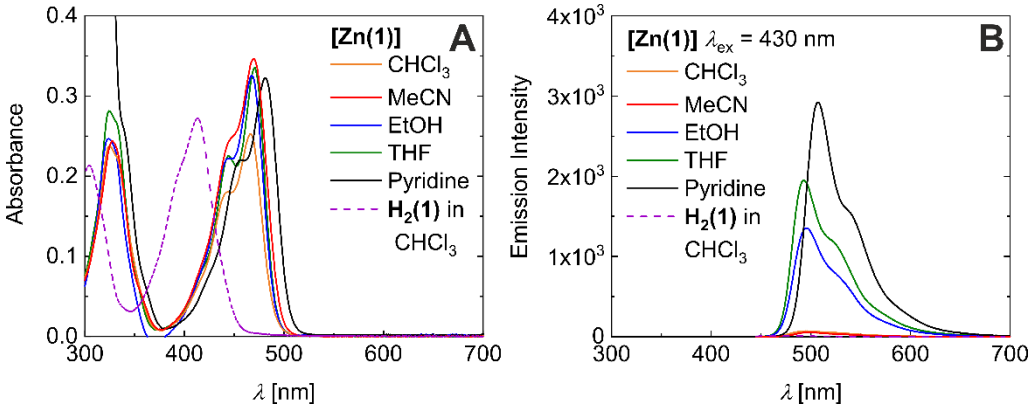

Figure 3. Absorbance (A) and emission (B) spectra of **[Zn(1)]** in $CHCl_3$, MeCN, EtOH, THF, and pyridine (7 x 10^{-6} M).

Intriguingly, **[Zn(1)]** shows weak fluorescence in $CHCl_3$, that is in a non-coordinating environment (λ_{Em} = 495 nm; $\Phi_F \approx 0.004$; all reported quantum yields are relative to **[Zn(1)]** in pyridine by the comparison of the absorbance corrected integrated emission intensity). Similar observations hold for **[Zn(2)]** and **[Zn(3)]**, with somewhat smaller quantum yield Φ_F of the latter. By contrast the free ligands are essentially silent under the same conditions ($\Phi_{Em} \approx 10^{-4}$); it is noted that the salicylic analogue of ligand (**1**) supports fluorescence with Φ_{Em} = 0.017.[15] The spectra of all zinc(II) complexes indicate partly resolved vibrational structure, both in absorption and in emission. An energy spacing of the vibrational progression by $\Delta_{vib}E \approx 1100$ cm^{-1} points to a leading role of chelate skeletal modes. This assignment is supported by analysis of DFT-derived harmonic frequencies (see Fig. S16 in the SI and animated gif).

Quite generally zinc complexes of planar-directing N_2O_2 ligands show significant solvatochromism in both, absorption and emission.[8b,8e] Different from these literature precedents, a cursory solvent scan shows that the absorption spectra of unit **[Zn(1)]** are largely indifferent to solvent variation with respect to energy and band shape (Fig. 3A). It is only in neat pyridine that absorption is affected. Notwithstanding the almost invariant absorption spectra, however, emission properties of **[Zn(1)]** vary substantially with solvent (see Figure 3B). While emission is very weak in chloroform and acetonitrile ($\Phi_{Em}(CHCl_3/MeCN) \approx 0.004$), it is greatly enhanced in EtOH and THF ($\Phi_{Em}(EtOH) \approx 0.07$ and $\Phi_{Em}(THF) \approx 0.10$) and reaches its maximum in neat pyridine ($\Phi_{Em}(Py) \approx 0.15$), indicating a steering role of the Lewis basicity. That is, coordination of Lewis-basic solvent molecules to the Lewis-acidic zinc center must be considered as the underlying molecular factor that switches on fluorescence in **[Zn(1)]**. As a matter of fact, fluorescence of **[Zn(1)]** which is silent in acetonitrile, can be increased successively through addition of water (see Figure S17 in the SI). Increasing the water fraction up to 50% results in a quantum yield increase up to $\Phi_{Em}(MeCN/H_2O\ 1/1) \approx 0.013$.

For instance, as shown in Figure 4A, titration of iso-concentrated solutions in $CHCl_3$ of **[Zn(1)]** with pyridine yields a continuous red-shift by up to 15 nm (see Fig. S15A/B in the SI for titrations of **[Zn(2)]** and **[Zn(3)]**, see Figure S18 for photographs), coupled to an intensity variation between 3.6 x 10^4 cm^{-1} M^{-1} < ε_M < 4.6 x 10^4 cm^{-1} M^{-1}. (see Fig. 4A). Fluorometric titration with the stronger base pyridine likewise shows a continuously enhanced emission for **[Zn(1)]** and **[Zn(2)]** which saturates only at the highest pyridine loads (see Fig. 4B and Figs. S15C in the SI). Fluorescence excitation spectra are indifferent to the observation wavelength and quantitatively map the absorption spectrum across the entire UV-Vis range (red in Fig. 4C, Figure S15E/F in the SI). Thereby, the pyridine-dependent red shift in absorption is compensated by a parallel red shift in emission so that the Stokes-shift of $\Delta_{Stokes}E \approx 1100$ cm^{-1} is preserved. Likewise, the coincidence of absorption and fluorescence excitation spectra (deviation at λ < 330 nm is due to uncompensated absorption by excess pyridine) and the vibrational structure of the diagnostic bands are maintained nearly constant (see Fig. 4D and Figure S15E in the SI).

DFT and wave-function theory analysis of the electronic structure. The nature of the leading optical transition of the zinc complexes has been addressed by means of (time-dependent) density-functional theory and wave function-based approaches. Complete active space self-consistent field, CASSCF, calculations were performed for the **[Zn(1)py]** complex, with an active space comprising the entire system of π-orbitals and their electrons, CAS(18,16). This represents the main orbital system responsible for the luminescence process. The lowest two singlet spin states (S_0 and S_1 states) and the lowest triplet spin state (T_1) wave functions have been optimized at the CASSCF level of theory, followed by a multiconfiguration pair-density functional theory approach (MC-PDFT) for treating dynamic correlation effects outside the chosen active space.[17] The singlet state calculations were performed at the DFT optimized geometry (pertinent metrics in Tables S5/6, SI). Triplet spin state calculations were

performed both at the optimized triplet geometry (*adiabatic excitation*) and at the singlet geometry (*vertical excitation*).

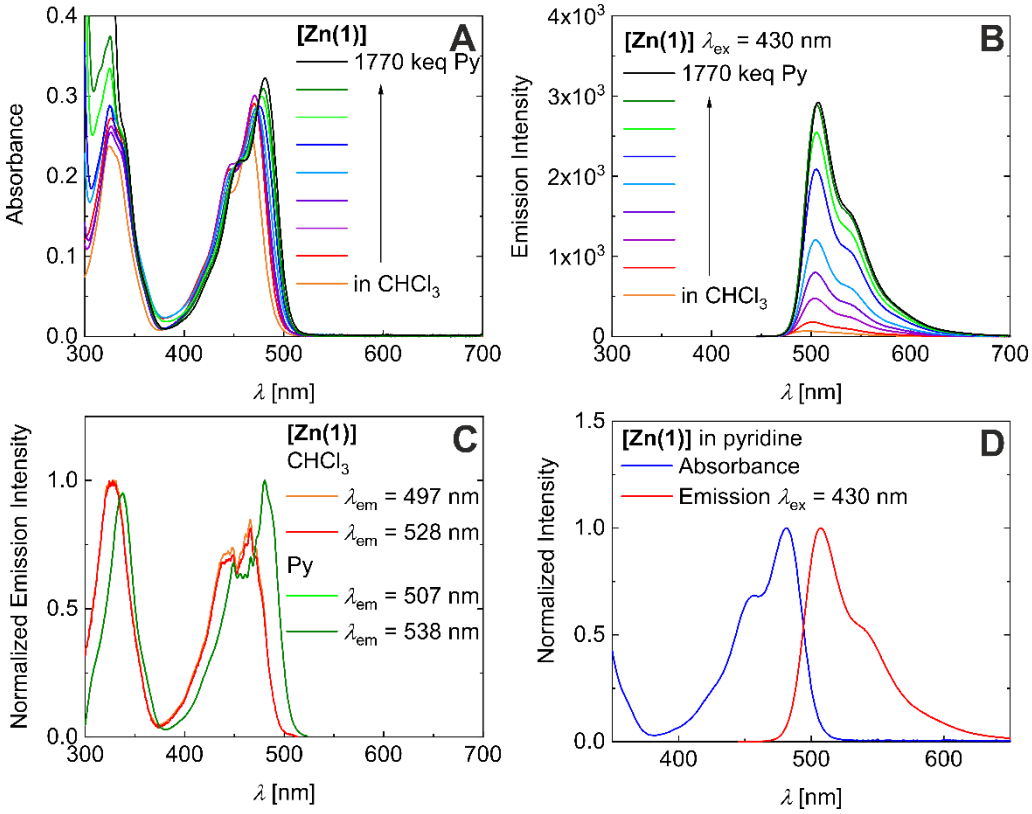

Figure 4. Chloroform/pyridine series: Absorption spectra of **[Zn(1)]** (**A**). Emission spectra of **[Zn(1)]** (λ_{exc} = 430 nm; **B**). Fluorescence excitation spectra of **[Zn(1)]** (**C**). Absorbance and emission spectra of **[Zn(1)]** in pyridine (**D**).

Table 2. Medium dependence of the $S_0 \rightarrow S_1$ transition of **[Zn(1)]** from experiment and theoretical modelling (λ_{max} [nm]; ε_{max} [10^4 M^{-1} cm^{-1}]).

	Experimental		Theoretical [a]		
Medium	λ_{max}	ε_{max}	λ_{max}	f_{osc}	Nature
chloroform	466	3.4	414 (487) [b]	0.784 [b]	$H_2 \rightarrow L$ (34%); $H \rightarrow L$ (59%)
			433 [c]	1.244 [c]	$H_2 \rightarrow L+1$ (44%); $H \rightarrow L$ (39%)
acetonitrile	469	5.0	430 [d]	0.782 [d]	$H \rightarrow L$ (92%)
acn/water (1:1)	467	4.4	426 [d]	0.791 [d]	$H \rightarrow L$ (92%)
EtOH/MeOH	467	4.6	427 [d]	0.746 [d]	$H \rightarrow L$ (90%)
THF	471	4.8	430 [d]	0.726 [d]	$H \rightarrow L$ (90%)
pyridine	481	4.6	440 (512) [d]	0.673 [d]	$H \rightarrow L$ (91%)

[a] On the TPSSh/TZVP level of theory; in parentheses: $S_0 \rightarrow S_1$ transition as predicted by MC-PDFT. [b] *hypothetic* CN 4 species. [c] dimeric species, **$[Zn(1)]_2$**. [d] CN 5 species with axial solvent.

The photophysics of **[Zn(1)X]** is invariably centered at the equatorial ligand. Variation of the axial ligand, X, does not considerably affect the transition frequency, in neither experiment nor theory (see Table 2). MC-PDFT calculations on **[Zn(1)py]** predict the $S_0 \rightarrow S_1$ transition at 512 nm, while DFT predicts the same transition at 440 nm, both in fair agreement with the experimental value (481nm) (see Table 2). TD-DFT tends to systematically

overestimate the energy of the leading Vis transition in the entire ligand-substitution series **[Zn(1)X]** (X: H_2O; ROH; pyridine; average deviation over five-coordinate complexes, $\Delta v = 1700\ cm^{-1}$), while MC-PDFT underestimates the transition energy for **[Zn(1)py].** Nonetheless, our theoretical predictions match the overall pattern and intensities in the experimental data.

Both at DFT and CASSCF level of theory, the HOMO and the LUMO are residing predominantly on the ligand (only at DFT level a very slight contribution of zinc d_{z2} features in the HOMO), yet with distinctly different local weights. The HOMO subsumes contributions of the ligand π-backbone and the σ-bound donors, whereas the LUMO is more localized on the dinitrile moiety. As a consequence, optical excitation in **[Zn(1)py]** leads to a charge shift toward the dinitrile site, rendering the excited state intra-ligand CT-like. Similar conclusions had been drawn previously in studies of the closely related congener **[Zn(sal)py]**, which derives from an enole/imine ligand based on salicylic aldehyde. In keeping with X-indifferent transition energies, the axial ligand does not feature significantly in the frontier molecular orbitals, as exemplarily shown in Figure 5 for **[Zn(1)py]** (data of the entire X-series is summarized in Fig. S19 in the SI). The optimized CASSCF natural orbitals for all states are similar to each other and to the Kohn-Sham-orbitals derived from DFT. They are reported in Figure S20 in the Supporting Information. As for the KS-orbitals, the CAS natural orbitals do not show any significant admixture from the pyridine. This indifference is supported by a very mild coordination-induced shift in the transition energies. For instance, MC-PDFT predicts the $S_0 \rightarrow S_1$ transition at 487 nm for the hypothetical four-coordinate model system **[Zn(1)]**, with no axial ligands. This formal effect of axial ligation on the energy of the $S_0 \rightarrow S_1$ transition in **[Zn(1)py]** is in the range of ~1000 cm^{-1}. With respect to the four-coordinate model compound **[Zn(1**)] a very similar coordination-induced red-shift by ~1400 cm^{-1} can be extracted from the TD-DFT data. Even smaller red-shifts of 700 – 900 cm^{-1} are induced by the weaker Lewis-bases (see Table 2). N_2O_3 coordination inherent to the dimeric complexes **[Zn(1)]$_2$** likewise results in a red-shifted $S_0 \rightarrow S_1$ transition. It is predicted at ≈ 430 nm, irrespective of dimer structure (see also Discussion below).

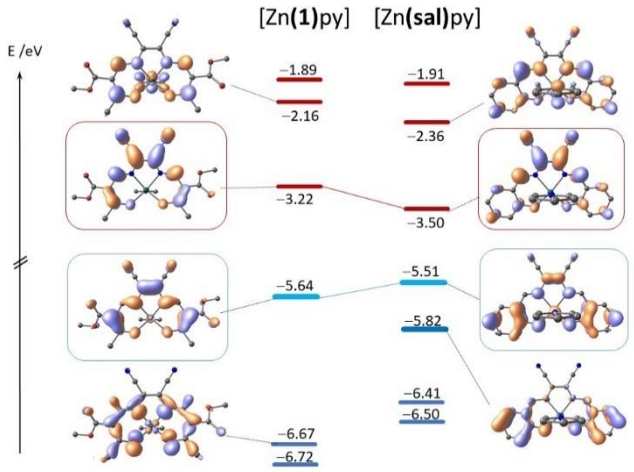

Figure 5. DFT-derived frontier MOs of five-coordinate zinc complexes (**[Zn(sal)py]** denotes an analogue derived from salicylic aldehyde; blue: occupied; red: virtual; HOMO and LUMO are highlighted.

Overall, both methods yield consistent results concerning the nature and energies of electronic states and transitions in the five-coordinate species. It is not uncommon that KS-DFT and the subsequent TD-DFT are able to describe excited states (here, the S_1 state) with a reasonable level of accuracy. This success comes necessarily somewhat surprising with a view to the fact that neither a bi-configurational wave function nor spin-adaptation is enforced by the method so that often unphysical eigensolutions to the Schrödinger equation (not spin eigenstates) are received. Nonetheless, KS-DFT can predict accurate energetics, in virtue of the fact that DFT relies on correct local spin-densities and not to the detailed structure of the wave function. Given the widespread utilization of KS-DFT also beyond its inherent single-reference limits, this aspect is discussed in the following. A more detailed treatment is given in Reference [17c].

Inspection of the CAS wave functions of the S_0 and S_1 states of **[Zn(1)py]** clearly corroborates the ILCT nature of the $S_0 \rightarrow S_1$ transition involving a HOMO to LUMO single excitation, adding value to our DFT computations. Both S_0 and S_1 wave functions are predominantly single-reference. The leading contribution to the S_0 state (79% weight) is the closed-shell configuration (single-reference) found also by KS-DFT for the same state. In the lowest excited singlet state an electronic configuration corresponding to the HOMO-to-LUMO one-electron excitation dominates with a weight of 73%. It is important to point out here that while the S_1 wave function is predominantly single-configurational (in terms of spin-adapted configuration state functions, CSFs), it is inherently bi-configurational.

That is, the two unpaired electrons residing in the HOMO and the LUMO are precisely coupled to a singlet spin state, $(a_H^{\alpha})^{\dagger}(a_L^{\beta})^{\dagger} - (a_H^{\beta})^{\dagger}(a_L^{\alpha})^{\dagger}$ (here H and L refer to HOMO and LUMO respectively). Thus, while both states can be considered single-reference, the S_1 excited state requires a more careful theoretical treatment, to ensure the correct spin-symmetry and to correctly capture electron correlation effects. These aspects are explicitly considered in the CASSCF/MCPDFT methodology, due to the multi-configurational character of the method, and their formulation in a spin-adapted basis (via the graphical unitary group approach, GUGA, algorithm).[18]

The MC-PDFT-derived vertical and adiabatic singlet-triplet gaps of **[Zn(1)py]**, $\Delta_{S/T}E$, are reported in the Jablonski diagram in Figure 6a; they are given in terms of the $S_0 \rightarrow T_1$ transition energies at the relaxed geometry of S_0 (vertical excitation) and T_1 (adiabatic excitation). Close-lying excited singlet and triplet states are generally taken as a basic requirement of rapid and efficient intersystem crossing, which would competitively limit the fluorescence quantum yield. A vertical gap of $\Delta_{S/T}E$ = 2.14 eV places the triplet state only 0.28 eV below the computed energy of the Franck-Condon state, that is, relative to S_1 in an excited vibronic state. In the relaxed geometry of T_1 the somewhat smaller adiabatic gap of $\Delta_{S/T}E$ = 1.97 eV arises, concomitant with a slightly widening gap between S_1 and T_1. Nevertheless, these calculations indicate an efficient ISC to the triplet state as the reducing factor of the fluorescence quantum yield. In the related zinc(II) system **[ZnTPP**] (TPP: tetraphenylporphine), fluorescence and phosphorescence have been recorded at 600 nm and ca. 780 nm (77 K), respectively, giving an upper limit for the S_1-T_1 gap of 0.48 eV.[19] In keeping with the narrow S_1-T_1 gap, a large triplet quantum yield of 0.88 was observed.

For comparison we plot in Figure 6b the data that derive from KS-DFT and TD-DFT. These are in qualitative agreement with the MC-PDFT values, but indicate larger S_1-T_1 splitting. We believe that a gap of 1.3 eV is hardly in agreement with efficient intersystem crossing.

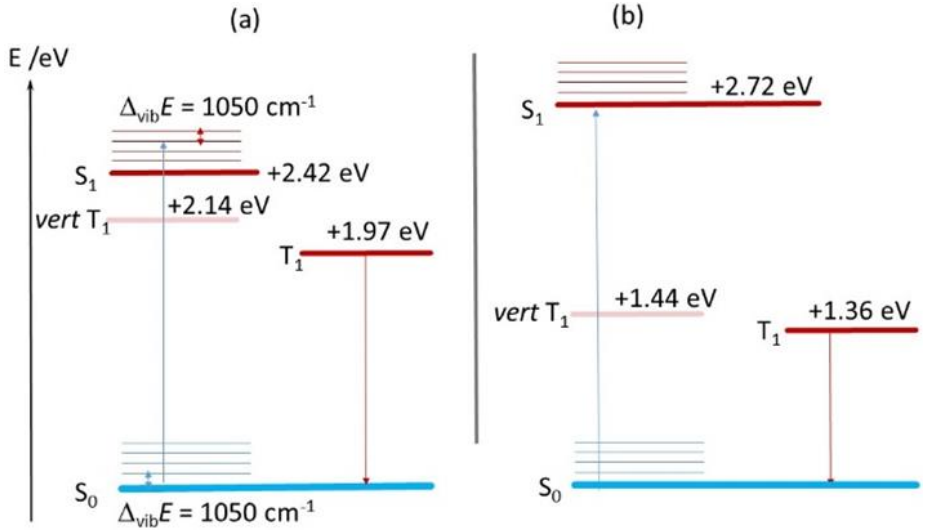

Figure 6. Jablonski diagrams of **[Zn(1)py]**; (a) data from MC-PDFT (ANO-RCC-VDZP); vibrational splitting $\Delta_{vib}E$ from experiment; (b) data from KS-DFT and TD-DFT ($S_0 \rightarrow S_1$) (TPSSh/TZVP).

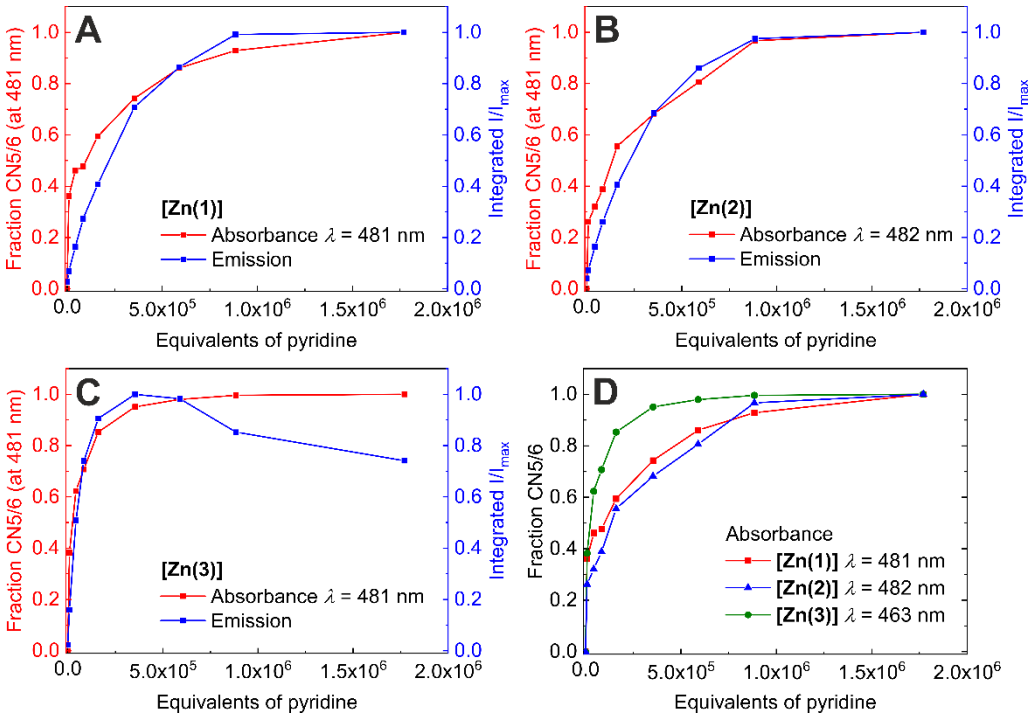

Figure 7. Fraction γ(CN5/6) of **[Zn(1–3)]** calculated by (A-A_{min})/(A_{max}-A_{min}) and integrated emission intensity I/I_{max} vs equivalents of pyridine (**A**: **[Zn(1)]**; **B**: **[Zn(2)]**; **C**: **[Zn(3)]**). **D** Comparison of fractions γ(CN5/6) of **[Zn(1–3)]**.

In agreement with experiment the Vis transition of **[Zn(sal)py]** (λ_{DFT} = 565 nm; λ_{exp} = 560 nm[16]) is predicted at significantly smaller energy than in **[Zn(1)py]** (λ_{DFT} = 440 nm; λ_{exp} = 481 nm). This tendency is maintained in the (*hypothetical*, see discussion) planar CN 4 species and is reflected by the shrinking HOMO-LUMO gap of **[Zn(sal)py]**. The presence of additional phenolate-borne π-donor states in the latter gives rise to further Vis transitions at higher energy that are clearly absent in **[Zn(1)py]**. Nevertheless, both complex families share similar optoelectronic properties, in a qualitative sense; that is, conserved nature and intensity of the leading excitation and significant CT-state emission with minor Stokes-shift. As is detailed below, however, they differ substantially in quantitative terms, with respect to their affinity for Lewis bases.

Speciation-dependent Emission Properties. To discuss the optical phenomena in more quantitative terms, the concentration dependence in the spectroscopic titrations with pyridine has been analyzed. Simultaneous plots of the integrated emission intensity and the differential changes of absorptivity (abstracted in terms of speciation; that is, reporting the fraction CN 5/6) as a function of pyridine concentration are shown in Figure 7.
As a first result, the above Lewis-base hypothesis is corroborated by the higher affinity for pyridine expressed by **[Zn(3)]**. Bearing electron withdrawing CF_3 substituents, **[Zn(3)]** is set apart quantitatively of the other zinc complexes in this study. With respect to **[Zn(1/2)]** the absorbance and emission bands of **[Zn(3)]** are all blue-shifted by approximately 15 nm (see Figure S15B/D/F in the SI). These shifts to larger energy reflect the stabilized Schiff-base borne donor levels (see MO diagram in Fig. S21 in the SI). They further support the ILCT character of the underlying transitions. As a more diagnostic effect of enhanced Lewis acidity, the pyridine-dependent spectral evolution of **[Zn(3)]** saturates above approximately 590 keq, whereas much larger amounts are necessary with **[Zn(1/2)]** (see Figure 7D). The experimentally observed order of affinity is well captured by DFT model calculations, assuming axial coordination of free planar species. In agreement with experiment, association is more exothermic in **[Zn(3)]** than in **[Zn(1)]**; the computed difference amounts to ca. 8 kJ mol^{-1}. Similarly, enhanced affinity for Lewis-bases has been recently reported for nickel(II) complexes of CF_3-decorated ligands.[20]

[Zn(1)] + py → **[Zn(1)py]**; $\Delta_{DFT}E$ = □110.2 kJ mol^{-1} (1)
[Zn(3)] + py → **[Zn(3)py]**; $\Delta_{DFT}E$ = □118.4 kJ mol^{-1} (2)
[Zn(sal)] + py → **[Zn(sal)py]**; $\Delta_{DFT}E$ = □101.1 kJ mol^{-1} (3)

Reaction energies of the Lewis acid-base association of pyridine with (*hypothetical*) planar zinc complexes are all highly negative, indicating a significant thermodynamic driving force even if unfavorable entropies are considered

(eq 1-3). It is of particular importance for the following argumentation to note that computed Lewis-base affinities of **[Zn(1)]** are *larger* than that of the known system **[Zn(sal)]**, $\Delta\Delta_{LB}E = \Delta_{LB}E$(**[Zn(1)]**) □ $\Delta_{LB}E$(**[Zn(sal)]**) ≈ □9 kJ mol^{-1} (for X = MeCN, pyridine, THF). That is, according to the chemistry indicated in eq 1-3 we must expect **[Zn(1)]** and **[Zn(3)]** to be more potent Lewis acids than **[Zn(sal)]**.
In clear contrast with this statement is the drastically smaller affinity of **[Zn(1)]** and **[Zn(3)]** toward axial ligation observed in experiment. Whereas ligation of **[Zn(sal)]** and derivatives thereof has been reported to saturate already at slightly to modestly super-stoichiometric doses of pyridine (2-10 eq),[8b] *all* complexes **[Zn(1–3)]** in the present study require pyridine doses that are higher by a factor of >> 10^4! Therefore, our analysis of ligation is clearly in error in -at least- one central aspect, notwithstanding that our theoretical modeling proved reliable otherwise. For instance, speciation in solution has been silently assumed to be identical for **[Zn(sal)]** and **[Zn(1–3)]**. As we discuss in the following, this assumption is most likely incorrect.

There is general agreement that, in the presence of donor molecules, one or two additional axial ligands will saturate the Lewis-acidic center of hypothetic four-coordinate zinc complexes as is implied by eq 1-3. In the absence of potent donors self-complementary stacking of such zinc(II) units occurs to yield dimers with a Zn_2O_2 core.[8] Dimeric crystal structures with a Zn_2O_2 core have been reported for several derivatives of the *salophen* type. Such dimeric structures are generally found to have reduced fluorescence quantum yields, whereas the on-switch of fluorescence in the presence of Lewis-bases has been interpreted in terms of base-induced de-aggregation. Stacking into dimers in non-coordinating media was likewise suggested to reduce fluorescence in *malnant* derivatives with maleodinitrile backbones.[8d] The ligation equilibria of **[Zn(sal)]** could be convincingly treated in terms of three-component models, yielding very large equilibrium constants for both, the dimerization step and the ligation of the sub-coordinate monomer (eq 4-5). The solution successively moves from one *single* non-fluorescent species to one *single* fluorescent species.

2 **[Zn(sal)]** → **[Zn(sal)]$_2$** $K_{dim} \approx 10^8$ M^{-1} (4)
[Zn(sal)] + py→ **[Zn(sal)py]** $K_{py} \approx 10^5$–10^6 M^{-1} (5)

Different from **[Zn(sal)]**, however, there is no such simple correlation for **[Zn(1–3)]**: Closer inspection of the low-concentration sections of the plots in Figure 7A/B reveals a lack of proportionality between both phenomenological parameters. In particular, the plot in Figure 8 of the normalized integrated emission intensity *vs* the CN 5/6 molar fraction of **[Zn(1–3)]** reflects pyridine-dependent transformations among (at least) four different species, from which (at least) the first two are fluorescence-silent. The close similarity of **[Zn(1–3)]** in the plot of Figure 8 points to an overall conserved phenomenology among all three compounds.

[Zn(1–3)]$_2$ + py → **[Zn(1–3)]$_2$ · py** (6)
[Zn(1–3)]$_2$ · py + py → 2 **[Zn(1–3)(py)]** (7)
2 **[Zn(1–3)(py)]** + 2 py → 2 **[Zn(1–3)(py)$_2$]** (8)

The first chemical step obviously connects these non-fluorescent species; notably almost one third of the overall absorption change is involved in this step, whereas there is hardly any increase in emission. In accordance to previous findings of fluorescence-silent stacked dimers,[8b,8d] it appears reasonable to ascribe the lack of fluorescence to the dimeric nature of *both* species (eq 6); see Discussion below. With further increase of the pyridine concentration beyond 8.8 keq, emission enhancement and absorption changes are proportional (rising branch in Figure 8). We attribute this step to the coordination of a second pyridine to the dimer that results in destacking of the dimers, concomitant with the successive formation of fluorescent monomeric **[Zn(1–3)py]** (equation 7). Finally, evolution of both, absorption and emission, tends to saturate for **[Zn(1–2)py]** at high pyridine doses. While the overall curve shape is close-to-identical also for **[Zn(3)]**, emission here even decreases in presence of high doses of pyridine. We associate this unique behavior with the enhanced Lewis-acidity of **[Zn(3)]** which allows for the formation of six-coordinate species (eq 8) as seen also in the solid state (Figure 1). While we cannot judge with definity, the decreased emission efficiency of six-coordinate species may be associated with the higher flexibility of the octahedral coordination sphere due to the intrinsically longer Zn-N/O bonds. The coordination of the second pyridine might also result in a decreased singlet-triplet gap leading to emission quenching, which was found indeed in DFT calculations (see Figure S23 in the SI). With a view to the close-to-identical curve progression in Figure 8, the lack of a similar emission decrease in the case of **[Zn(1/2)]** simply reflects the reduced affinity of the zinc centers towards six-coordination.

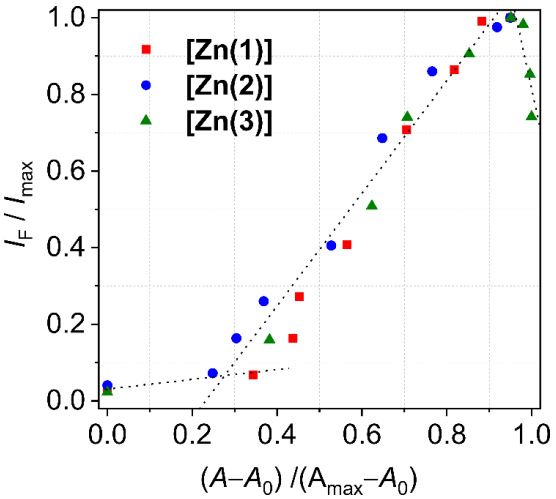

Figure 8. Correlation of pyridine-dependent absorption and emission changes. Plot of the normalized integrated emission intensity vs the CN5/6 molar fraction of **[Zn(1–3)]**. $Fraction_{CN5/6} = (A – A_0)/(A_{max} – A_0)$. $Fraction_{5/6}$ of **[Zn(1/2)]** scaled by a factor of 0.95.

The *seemingly* reduced Lewis-acidity of **[Zn(1–3)]** and the occurrence of a pyridine containing dimeric species in the correlation plot indicate the formation of dimers with a strongly enhanced stability compared to **[Zn(sal)]**. As **[Zn(1–3)]** are actually identified as stronger Lewis-acids by DFT calculations, the reduced Lewis-acidity cannot be assigned to a molecular origin. This intrinsic enhanced metal-borne acidity must be overridden by an additional ligand-borne effect, which massively affects the structure of the dimer. While direct structural evidence is not yet available from experiment, a reasonable stacked structure of **[Zn(sal)]** is shown in Figure 9A which derives from DFT optimization. The computed metrics of the Zn_2O_2 core are highly similar to the reported crystal structures of *salophen*-type complexes.[21] Details of all optimized structures are summarized in Table S7 in the SI. In particular, the short axial Zn-O distance of 2.15 Å indicates tight binding within the dimers; electronic reaction energies of the dimerization equilibrium amount to -16 kJ mol^{-1}. Very similar structures could be extracted from optimization of Zn_2O_2-bound dimers of **[Zn(1)]**, with similar energies of dimerization.

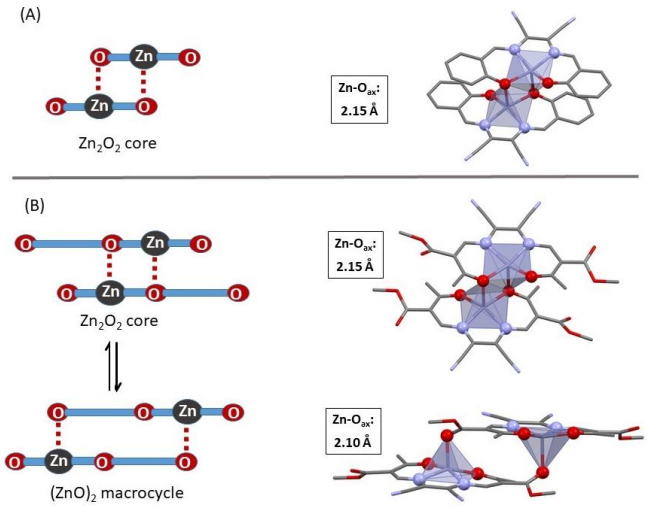

Figure 9. (A) Dimer speciation of **[Zn(sal)]$_2$** (left) and its DFT-optimized structures with pertinent metrics (right). (B) Dimer speciation of **[Zn(1–3)]$_2$** (left) and its DFT-optimized structures with pertinent metrics (right).

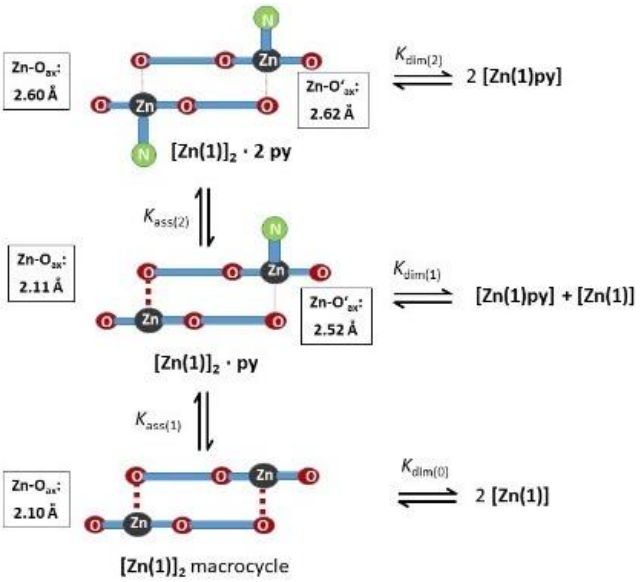

Figure 10. Dimer speciation of **[Zn(1-3)]$_2$** upon successive addition of axial N-donors.

Most importantly, however, these Zn_2O_2-core dimers are not the minimum structures in the case of **[Zn(1–3)]**. By contrast, DFT calculations suggest the presence of a completely different stacking motif to manifest the energy minimum, as shown in Figure 9B. In these $(ZnO)_2$ macrocycles, ligand-appended carbonyls saturate the N_2O_3 coordination sphere of zinc to establish fully relaxed square-pyramidal environments on both centers. A somewhat related constellation has been observed by Weber *et al*. in the solid-state structure of some iron(II) complexes of this general ligand type.[22] In the cited system, the axially arranged carbonyls rather assist coordination, given the long M-O distance of 2.70 Å. In **[Zn(1–3)]**, tight axial binding is indicated by short Zn-O_{ax} bond lengths of 2.10 Å, which are even shorter than in the reported and computed dimers of **[Zn(sal)]**. Favorable dispersive interactions support the laterally shifted dimer structure. Both aspects sum up in a strongly increased stability compared to the Zn_2O_2 dimer pertinent to **[Zn(sal)]**. Computed energies of dimerization are in favor of the macrocyclic **$(ZnO)_2$** dimer by -20 kJ mol^{-1}. In terms of a greatly enhanced $K_{dim(0)}$ (Figure 10), the structure and stability of the dimer of **[Zn(1–3)]** is most likely the reason for the lower sensitivity of **[Zn(1–3)]** towards axial donors. Intriguingly, the dimeric structure survives even upon coordination of one axial donor. While the *trans*-N located bond in the resulting pseudo-octahedral N_3O_3 site of **[Zn(1–3)]** · **py** is clearly elongated (d(Zn-O_{ax} = 2.52 Å), the dimer as such stays intact (equation 7, see also Figure 10). It is only after coordination of the second pyridine molecule that both axial Zn-O_{ax} are elongated. The concomitant loss of binding energy and dispersive interactions serve to break the dimer structure.

Conclusions

The family of planar zinc(II) complex platforms, **[Zn(1–3)]**, based on planar-directing tetradentate Schiff base-like ligands with appended nitrile groups supports *turn-on* fluorescence behavior, sensitive to axial ligation with potent Lewis bases. Efficient emission is observed in neat pyridine (Φ_{Em} = 0.15), methanol and tetrahydrofuran, but absent in non-coordinating solvents such as chloroform. The strong correlation of the emission intensity with the basicity of the solvents reflects solvent-dependent coordination of zinc. In keeping with this conclusion, five-coordinate complexes fully dominate the solid-state structures of **[Zn(1–2)X]**, with **X** being an axially coordinating Lewis-base. It is noted that the introduction of the electron withdrawing substituent CF_3 in **[Zn(3)]** results in a favored ligation due to an increase of the Lewis acidity of the zinc(II) metal center, yielding six-coordinate zinc in the solid state.

DFT and CASSCF/MC-PDFT identify the $S_0 \rightarrow S_1$ transition as a single-electron HOMO-LUMO intra-ligand charge transfer, in which transition charge density is shifted from the chelate cycle to the dinitrile substituents. While the overall optical spectroscopic features of **[Zn(1–3)X]** comply with the established stacking/destacking hypothesis of zinc(II)-based fluorescence sensors in qualitative terms, a massive deviation is noticed in terms of a quantitative treatment. While only 2-3 equivalents of pyridine were reported to switch-on fluorescence in the closely related congener **[Zn(sal)]**, a large excess of approximately 10^4 equivalents is required in the case of **[Zn(1–3)]**. This enormous difference in sensitivity cannot be traced to a respective divergence in Lewis acidity (KS-DFT calculations suggested an even stronger Lewis-acidity of **[Zn(1–3)]**). In fact, the higher intrinsic acidity of **[Zn(1–3)]** is hidden

through dimerization. KS-DFT calculations support a very stable stacking motif for **[Zn(1–3)]** which qualitatively differs from the Zn_2O_2 core of **[Zn(sal)]**.

The minor impact of the zinc(II) coordination environment on the absorbance behavior indicates that the metal center only indirectly influences the optical behavior through dimer formation. The close proximity in these zinc-mediated dimers might be the reason for the emission quenching in non-coordinating solvent and the turn-on effect upon destacking. This insight opens the way to consciously address different sensitivity areas upon tuning the dimer stability through introduction of sterically demanding substituents.

Experimental Section

Methoxymethylenemethylacetoacetate, ethoxymethyleneethylaceto-acetate, ethoxymethylene-1,1,1-trifluoroacetylacetone, and **H_2(2)** were synthesised as described in literature.[11,23] - Diaminomaleonitril (98%, Sigma Aldrich), *p*-toluenesulfonic acid (98%, Merck), and $Zn(OAc)_2 \cdot 2\ H_2O$ (97+%, Alfa Aesar) were used without further purification. Methanol, ethanol, THF, and pyridine were of analytical grade and used without further purification. Chloroform and acetonitrile were extracted with aqueous saturated $NaHCO_3$ solution and dried over $CaCl_2$. NMR spectra were recorded with a 500 MHz *Avance III HD* NMR spectrometer from Bruker. CHN analyses were measured with an Unicube from Elementar Analysen Systeme. The samples were prepared in a tin boat, sulfanilamide was used as standard and the samples measured at least twice. Mass spectra were recorded with a Finnigan MAT 8500 with a data system MASPEC II. IR spectra of the solid samples were recorded on a *Perkin Elmer Spectrum* 100 FT-IR spectrometer.

X-ray Structure Analysis. The X-ray analysis were performed with a Stoe StadiVari diffractometer using graphite-monochromated MoK_α radiation. The data were corrected for Lorentz and polarization effects. The structures were solved by direct methods (SIR-97)[24] and refined by full-matrix least-square techniques against Fo2–Fc2 (SHELXL-97).[25]All hydrogen atoms were calculated in idealized positions with fixed displacement parameters. ORTEP-III was used for the structure representation,[26] Mercury-3.10 to illustrate molecule packing.[27]

X-ray Powder Diffraction. Powder diffractograms were recorded with a STOE StadiP diffractometer using Cu Kα1 radiation with a Ge monochromator, and a Mythen 1K Stripdetector in transmission geometry.

Optical Measurements. Absorbance spectra were performed on a Cary 60 UV-Vis spectrometer from Agilent Technologies. Steady-state PL measurements were performed on a FP-8600 fluorescence spectrometer from JASCO that is equipped with a Xe lamp as excitation source. Time-resolved measurements were performed on a FluoTime 300 fluorospectrometer from PicoQuant, using a 405 nm diode laser for excitation (Coherent COMPASS 405-50 CW), which was controlled by the PDL 820 PicoQuant laser driver. Quantum yields were determined at room temperature using an integrating sphere and a Xe lamp as excitation source. All measurements were performed in quartz cells with a 1 cm lightpath from Hellma.

H_2(1). Diaminomaleonitrile (1.50 g, 13.88 mmol, 1 eq), methoxymethylene-methylacetoacetate (4.83 g, 30.53 mmol, 2.2 eq), and *p*-toluenesulfonic acid (0.13 g, 0.69 mmol, 0.05 eq) were dissolved in 37 mL MeOH. The red solution was heated under reflux for 5 h. After cooling at room temperature overnight the orange precipitate was filtered off and washed with MeOH. Yield: 2.18 g (44 %). ^{1}H NMR (500 MHz, DMSO, 25°C): δ = 8.11 (s, 2 H, NC–H); 3.74 (s, 6 H, $–CH_3$); 2.44 (s, 6 H, $–CH_3$) ppm. MS (DEI-(+), 70 eV): m/z = 360 (M+, 36%). $C_{16}H_{16}N_4O_6$ (360.33 g/mol) found (calculated): C 53.18 (53.33); H 4.33 (4.48); N 15.31 (15.55)%. IR: $\tilde{\upsilon}$ = 2954 (s, C–H), 2228 (s, C≡N), 1719 (s, C=O), 1585 (s, C=O) cm^{-1}.

[Zn(1)(H_2O)(MeOH)]. H_2(1) (0.40 g, 1.11 mmol, 1 eq) and zinc(II) acetate dihydrate (0.32 g, 1.44 mmol, 1.3 eq) were dissolved in 40 mL MeOH. The solution was heated to reflux for 2 h. After cooling to room temperature and addition of 20 mL H_2O, the red crystalline precipitate was filtered off and washed with MeOH. Yield: 0.37 g (70%). ^{1}H NMR (500 MHz, DMSO, 25°C): δ = 8.51 (s, 2 H, NC–H); 3.69 (s, 6 H, $–CH_3$); 2.49 (s, 6 H, $–CH_3$) ppm. MS (DEI-(+), 70 eV): m/z = 422 (M+, 58%). $C_{17}H_{20}N_4O_8Zn$ (473.75 g/mol) found (calculated): C 42.97 (43.10); H 4.11 (4.26); N 11.98 (11.83)%. IR: $\tilde{\upsilon}$ = 3394 (b, O–H), 2954 (s, C–H), 2217 (s, C≡N), 1677 (s, C=O), 1574 (s, C=O) cm^{-1}.

[Zn(2)(H_2O)$_{1.5}$]. H_2(2) (0.40 g, 1.03 mmol, 1 eq) and zinc(II) acetate dihydrate (0.29 g, 1.34 mmol, 1.3 eq) were dissolved in 40 mL MeOH. The solution was heated to reflux for 2 h. After cooling to room temperature and addition of 20 mL H_2O, the orange precipitate was filtered off and washed with MeOH. Yield: 0.23 g (47%). ^{1}H NMR (500 MHz, DMSO, 25°C): δ = 8.53 (s, 2 H, NC–H); 4.16 (q, $^3J(CH_2–CH_3)$ = 7.0 Hz, 4 H, $–CH_2$); 2.49 (s, 6 H, $–CH_3$); 1.25 (t, $^3J(CH_2–CH_3)$ = 7.0 Hz, 6 H, $–CH_3$) ppm. MS (DEI-(+), 70 eV): m/z = 450 (M^+, 100%). $C_{18}H_{21}N_4O_{7.5}Zn$ (478.77 g/mol) found (calculated): C 45.37 (45.16); H 4.24 (4.42); N 11.68 (11.70)%. IR: $\tilde{\upsilon}$ = 3311 (b, O–H), 2987 (s, C–H), 2217 (s, C≡N), 1674 (s, C=O), 1583 (s, C=O) cm^{-1}.

[Zn(3)(H_2O)(EtOH)]. Diaminomaleonitrile (0.05 g, 0.46 mmol, 1 eq), ethoxymethylene-1,1,1-trifluoroacetylacetone (0.21 g, 1.02 mmol, 2.2 eq), and zinc(II) acetate dihydrate (0.13 g, 0.60 mmol, 1.3 eq) were dissolved in 2.5 mL EtOH. The solution was heated to reflux for 2 h. After cooling to room temperature, 1 mL H_2O was added. After storing in the fridge overnight, the red precipitate was filtered off and washed with EtOH. Yield: 0.17 g (66%). ^{1}H

NMR (500 MHz, DMSO, 25°C): δ = 8.35 (s, 2 H, NC–H); 2.54 (s, 6 H, –CH_3) ppm. MS (DEI-(+), 70 eV): m/z = 498 (M^+, 30%), 429 (M^+-CF_3, 53%). $C_{18}H_{16}F_6N_4O_6Zn$ (563.72 g/mol) found (calculated): C 38.32 (38.35); H 2.84 (2.86); N 9.98 (9.94)%. IR: $\tilde{\upsilon}$ = 3511 (b, O–H), 3355 (b, O–H), 2987 (s, C–H), 2224 (s, C≡N), 1597 (s, C=O), 1538 (s, C=O), 1116 (s, C–F) cm^{-1}.

Computational Details

This section describes the most relevant details of DFT and CASSCF model calculations.

(TD-)DFT. Electronic structure calculations on the complexes have been performed through density-functional theory (DFT) methods using the ORCA program package.[28] For all optimizations triple-ξ-valence TZVP basis sets[29] were used with the generalized gradient approximated functional BP86.[30] Optimized complexes were verified as stationary points through the absence of imaginary modes in numerical frequency calculations. Molecular orbitals and electronic properties were extracted from single-point calculations in the optimized positions with the global hybrid functional TPSSh[31] and triple-ξ-valence TZVP basis sets. Grimme's third generation D3 correction of dispersion was used;[32] medium effects were approximated in a dielectric continuum approach (COSMO), parameterized for MeCN.[33] Coordinates of the computed structures are assembled in the SI file COORDINATES, frontier orbital landscapes are shown in Figures S19-S21/22 in the SI. For each complex the 70-80 lowest optical electronic transitions were assessed with ORCA implemented TD-DFT methods within the Tamm-Dancoff approximation.

CASSCF/MC-PDFT. Considering the marginal role of the closed-shell Zn(II) metal center in terms of correlation effect, as discussed above, the active space chosen for all CASSCF calculations contains MOs predominantly with character of the π-system of the tetra-dentate ligand, CAS(18,16), where the 16 orbitals are linear combinations of the 16 2p AOs on the conjugated system of the ligand. State-averaged calculations with 2 roots were performed for the singlet spin system (S_0 and S_1), while only the ground state for the triplet spin symmetry, T_1.
MC-PDFT has been largely demonstrated a good and cheap alternative to CASPT2 and it has been utilized as main method of choice in this investigation to recover dynamic correlation outside the active space. Within MC-PDFT the tPBE translated functional has been chosen, that in our experience outperforms the other translated functional available to date.
A basis set of generally contracted atomic natural orbital (ANO-RCC) type has been used for all atoms, obtained from the C,N,O(14s,9p,4d), H(8s,4p) and Zn(21s,15p,10d,6f) primitive functions, contracted to C,N,O(3s,2p,1d), H(2s,1p), Zn(5s,4p,2d,1f) functions, giving a basis set of split-valence double-ζ plus polarization quality (VDZP). This choice of basis set leads to a total of 577 basis functions for the **[Zn(1)py]** model system. Intermediate calculations in a minimal basis set (MB), with contraction scheme C,N,O(2s,1p), H(1s), Zn(4s,3p,1d), have been performed as aid in the choice of the active space for all model system and spin states. The basis set has been subsequently expanded to the VDZP and the MB optimized orbitals augmented and used as starting orbitals for the VDZP CASSCF(18,16) optimization. C1 point group symmetry has been utilized in line with the preceding DFT method. The evaluation of the electron repulsion integrals has been greatly simplified by means of the resolution-of-identity Cholesky decomposition technique, with a decomposition threshold of 10^{-4} a.u.

Acknowledgements

Financial supports from the Fonds der Chemischen Industrie (Kekulé-Stipendium), MINT-Lehramt Plus, German Research foundation (SFB840; project A10), the BayNAT program, the Max-Planck Society, and the University of Bayreuth are gratefully acknowledged. We thank Dr. Ulrike Lacher for the measurement of the mass spectra, Florian Puchtler for the measurement of the PXRD patterns. We thank Prof. Dr. Hans-Werner Schmidt for access to the fluorospectrometer for the steady-state measurements, Prof. Dr. Roland Marschall and Dr. Jana Timm for access to the FluoTime 300 fluorospectrometer for quantum yield determinations, and Armin Schuhmacher for the technical support on the local cluster used for the CASSCF/MC-PDFT simulations.

Keywords: Zinc • Fluorescence • Dimerization • Schiff base • CASSCF

[1] E. Coronado, *Nat Rev Mater* **2020**, *5*, 87–104.
[2] a) B. Sieklucka, D. Pinkowicz, *Molecular Magnetic Materials;* Wiley-VCH Verlag GmbH & Co. KGaA, Weinheim, Germany, **2017**; b) M. A. HALCROW, *Spin-Crossover Materials;* John Wiley & Sons Ltd, Oxford, UK, **2013**;
[3] a) S. Thies, H. Sell, C. Schütt, C. Bornholdt, C. Näther, F. Tuczek, R. Herges, *Journal of the American Chemical Society* **2011**, *133*, 16243–16250; b) M. Dommaschk, C. Schütt, S. Venkataramani, U. Jana, C. Näther, F. D. Sönnichsen, R. Herges, *Dalton transactions (Cambridge, England : 2003)* **2014**, *43*, 17395–17405;
[4] a) C. Lochenie, K. Schötz, F. Panzer, H. Kurz, B. Maier, F. Puchtler, S. Agarwal, A. Köhler, B. Weber, *Journal of the American Chemical Society* **2018**, *140*, 700–709; b) K. Senthil Kumar, M. Ruben, *Coordination Chemistry Reviews* **2017**, *346*, 176–205; c) C. Lochenie, K. G. Wagner, M. Karg, B. Weber, *J. Mater. Chem. C* **2015**, *3*, 7925–7935;
[5] a) C. Förster, K. Heinze, *Chemical Society reviews* **2020**, *49*, 1057–1070; b) O. S. Wenger, *Journal of the American Chemical Society* **2018**, *140*, 13522–13533; c) O. S. Wenger, *Chemistry (Weinheim an der Bergstrasse, Germany)* **2019**, *25*, 6043–6052;

[6] a) Y. Zhang, J. L. Petersen, C. Milsmann, *Journal of the American Chemical Society* **2016**, *138*, 13115–13118; b) C. Förster, K. Heinze, *J. Chem. Educ.* **2020**, *97*, 1644–1649; c) Y. Zhang, M. Schulz, M. Wächtler, M. Karnahl, B. Dietzek, *Coordination Chemistry Reviews* **2018**, *356*, 127–146; d) J. Xiong, K. Li, T. Teng, X. Chang, Y. Wei, C. Wu, C. Yang, *Chemistry (Weinheim an der Bergstrasse, Germany)* **2020**, *26*, 6887–6893;
[7] a) J. A. Marafie, D. D. C. Bradley, C. K. Williams, *Inorganic chemistry* **2017**, *56*, 5688–5695; b) J. Cheng, Y. Li, R. Sun, J. Liu, F. Gou, X. Zhou, H. Xiang, J. Liu, *J. Mater. Chem. C* **2015**, *3*, 11099–11110;
[8] a) M. K. Paul, Y. Dilipkumar Singh, N. Bedamani Singh, U. Sarkar, *Journal of Molecular Structure* **2015**, *1081*, 316–328; b) G. Consiglio, S. Failla, I. P. Oliveri, R. Purrello, S. Di Bella, *Dalton transactions (Cambridge, England : 2003)* **2009**, 10426–10428; c) D. Xie, J. Jing, Y.-B. Cai, J. Tang, J.-J. Chen, J.-L. Zhang, *Chem. Sci.* **2014**, *5*, 2318; d) G. Forte, I. P. Oliveri, G. Consiglio, S. Failla, S. Di Bella, *Dalton transactions (Cambridge, England : 2003)* **2017**, *46*, 4571–4581; e) G. Consiglio, I. P. Oliveri, S. Cacciola, G. Maccarrone, S. Failla, S. Di Bella, *Dalton transactions (Cambridge, England : 2003)* **2020**, *49*, 5121–5133; f) I. P. Oliveri, G. Malandrino, S. Di Bella, *Inorganic chemistry* **2014**, *53*, 9771–9777; g) M. Strianese, D. Guarnieri, M. Lamberti, A. Landi, A. Peluso, C. Pellecchia, *Inorganic chemistry* **2020**, *59*, 15977–15986;
[9] Y. Yao, H.-Y. Yin, Y. Ning, J. Wang, Y.-S. Meng, X. Huang, W. Zhang, L. Kang, J.-L. Zhang, *Inorganic chemistry* **2019**, *58*, 1806–1814.
[10] a) X. Yan, X. Song, X. Mu, Y. Wang, *New J. Chem.* **2019**, *43*, 15886–15891; b) S. M. Borisov, R. Pommer, J. Svec, S. Peters, V. Novakova, I. Klimant, *J. Mater. Chem. C* **2018**, *6*, 8999–9009; c) A. Steinegger, S. M. Borisov, *ACS omega* **2020**, *5*, 7729–7737;
[11] H. Kurz, G. Hörner, B. Weber, *Z. Anorg. Allg. Chem.* **2021**, *647*, 896–904.
[12] S. ALVAREZ, P. ALEMANY, D. CASANOVA, J. CIRERA, M. LLUNELL, D. AVNIR, *Coordination Chemistry Reviews* **2005**, *249*, 1693–1708.
[13] Z.-C. Wang, J. Chu, S.-Z. Zhan, *Acta crystallographica. Section E, Structure reports online* **2013**, *69*, m419.
[14] K. Ouari, A. Ourari, J. Weiss, *J Chem Crystallogr* **2010**, *40*, 831–836.
[15] J. Cheng, K. Wei, X. Ma, X. Zhou, H. Xiang, *J. Phys. Chem. C* **2013**, *117*, 16552–16563.
[16] F. Dumur, E. Contal, G. Wantz, D. Gigmes, *Eur. J. Inorg. Chem.* **2014**, *2014*, 4186–4198.
[17] a) L. Gagliardi, D. G. Truhlar, G. Li Manni, R. K. Carlson, C. E. Hoyer, J. L. Bao, *Accounts of chemical research* **2017**, *50*, 66–73; b) C. E. Hoyer, S. Ghosh, D. G. Truhlar, L. Gagliardi, *The journal of physical chemistry letters* **2016**, *7*, 586–591; c) G. Li Manni, R. K. Carlson, S. Luo, D. Ma, J. Olsen, D. G. Truhlar, L. Gagliardi, *Journal of chemical theory and computation* **2014**, *10*, 3669–3680;
[18] a) J. Paldus, *The Journal of Chemical Physics* **1974**, *61*, 5321–5330; b) J. Paldus, *J Math Chem* **2021**, *59*, 1–36; c) I. Shavitt, *Int. J. Quantum Chem.* **1977**, *12*, 131–148; d) I. Shavitt, *International Journal of Quantum Chemistry* **1978**, *14*, 5–32;
[19] a) D. J. Quimby, F. R. Longo, *J. Am. Chem. Soc.* **1975**, *97*, 5111–5117; b) A. Harriman, *J. Chem. Soc, Faraday Trans. 1* **1980**, *76*, 1978;
[20] H. Kurz, K. Schötz, I. Papadopoulos, F. W. Heinemann, H. Maid, D. M. Guldi, A. Köhler, G. Hörner, B. Weber, *Journal of the American Chemical Society* **2021**, *143*, 3466–3480.
[21] M. Martínez Belmonte, S. J. Wezenberg, R. M. Haak, D. Anselmo, E. C. Escudero-Adán, J. Benet-Buchholz, A. W. Kleij, *Dalton transactions (Cambridge, England : 2003)* **2010**, *39*, 4541–4550.
[22] B. Weber, I. Käpplinger, H. Görls, E.-G. Jäger, *Eur. J. Inorg. Chem.* **2005**, *2005*, 2794–2811.
[23] a) S. P. Singh, D. Kumar, *J. Chem. Res.* **1997**, 142–143; b) L. Claisen, *Justus Liebigs Ann. Chem.* **1897**, *297*, 1–98;
[24] A. Altomare, M. C. Burla, M. Camalli, G. L. Cascarano, C. Giacovazzo, A. Guagliardi, A. G. G. Moliterni, G. Polidori, R. Spagna, *J Appl Crystallogr* **1999**, *32*, 115–119.
[25] G. M. Sheldrick, *Acta crystallographica. Section A, Foundations of crystallography* **2008**, *64*, 112–122.
[26] a) M. N. Burnett, C. K. Johnson, *ORTEP-III: Oak Ridge Thermal Ellipsoid Plot Program for crystal structure illustrations;* Office of Scientific and Technical Information (OSTI), **1996**; b) L. J. Farrugia, *J Appl Cryst* **1997**, *30*, 565;
[27] C. F. Macrae, P. R. Edgington, P. McCabe, E. Pidcock, G. P. Shields, R. Taylor, M. Towler, J. van de Streek, *J Appl Crystallogr* **2006**, *39*, 453–457.
[28] F. Neese, *WIREs Comput Mol Sci* **2012**, *2*, 73–78.
[29] A. Schäfer, H. Horn, R. Ahlrichs, *The Journal of Chemical Physics* **1992**, *97*, 2571–2577.
[30] Becke, *Physical review. A, General physics* **1988**, *38*, 3098–3100.
[31] V. N. Staroverov, G. E. Scuseria, J. Tao, J. P. Perdew, *The Journal of Chemical Physics* **2003**, *119*, 12129–12137.
[32] a) S. Grimme, J. Antony, S. Ehrlich, H. Krieg, *The Journal of Chemical Physics* **2010**, *132*, 154104; b) S. Grimme, S. Ehrlich, L. Goerigk, *Journal of computational chemistry* **2011**, *32*, 1456–1465;
[33] A. Klamt, G. Schüürmann, *J. Chem. Soc, Perkin Trans. 2* **1993**, 799–805.

Entry for the Table of Contents

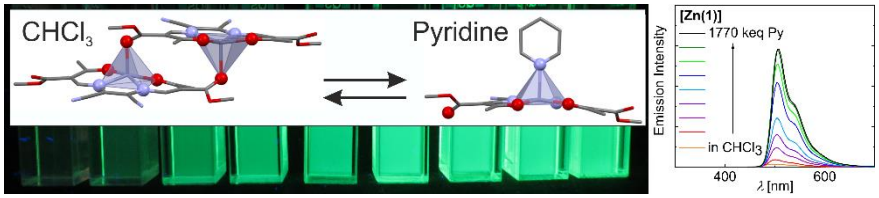

We synthesized three new zinc(II) coordination units based on Schiff base-like ligands equipped with nitrile groups. In non-coordinating solvents such as chloroform a near-to zero emission was observed, that increased drastically upon addition of the Lewis base pyridine (Φ = 15%). Interestingly, DFT calculations indicate that the intrinsically high Lewis-acidity of the zinc(II) metal center is hidden through formation of highly stable dimers.